Chapter

Digital Sorting of Optical Vortices in Perturbed Singular Beams

Alexander Volyar, Mikhail Bretsko, Yana Akimova and Yuriy Egorov

Abstract

The chapter provides a brief overview of shaping and measuring techniques of the vortex spectra (squared amplitudes and initial phases of vortex modes) including radial indices. The main physical mechanisms causing the formation of laser beams with a complex vortex composition, in particular, in biological media, are indicated, and the need for a digital analysis of vortex spectra is substantiated. It is the analysis of vortex spectra that allows us to find the orbital angular momentum and informational entropy (Shannon's entropy) of perturbed laser beams in real time. In the main part of the chapter, we consider in detail a new approach for measuring vortex spectra without cuts and gluing of the wavefront, based on digital analyzing high-order intensity moments of complex beams and sorting the vortex beam in computer memory sells. It is shown that certain types of weak local inhomogeneities cause a vortex avalanche causing a sharp dips and bursts of the orbital angular momentum spectra and quick ups and downs of the informational entropy. An important object of analysis is also the vortex spectra of beams scattered by simple opaque obstacles such as a hole, a disk, and a sector aperture.

Keywords: optical vortex, moment's intensity, orbital angular momentum, medical optics

1. Introduction

As is well known, optical vortices [1] accompany light scattering processes due to both simple and complex medium inhomogeneities (see, e.g., [2] and references therein). Scattered light carries a huge array of information, both on the composition and structure of scattering (diffraction) centers, and on the structure of the initial light beam. At the same time, optical information can be read off both by analyzing the frequency spectrum [3–5] and the spectrum of optical vortices [6, 7]. An important aspect of this problem is the study of biomedical objects [8, 9], for example, the composition of the blood or the reflection of a vortex beam from the skin surface [10] for express diagnostics of skin diseases. The fact is that a vortex beam scattered by the skin is transformed into a speckle-like structure resembling one that occurs when light passes through a medium with weak turbulence [11, 12]. At the same time, the speckle structure is formed by the skeleton of optical vortex array [13–15]. In turn, the analysis of such a complex vortex structure is conveniently carried out on the basis of vortex fractal techniques [16] (see also [17] and references therein). There are a variety of approaches for the fractal vortex models

of laser beams scattered by biological tissues [18, 19] based on the light scattering by nonspherical particles [20] that involves the representation of the wave field in terms of Legendre polynomials. However, a real optical experiment for measuring the vortex spectrum requires the use of particular approaches to the orthogonal basis for the scattered beam expansion in terms of special functions, which can differ significantly from the corresponding theoretical models.

The problem of using the properties of optical vortices in various areas of science and technology requires the development of reliable but simple techniques for measuring the spectrum of optical vortices in complex beams scattered by various objects. Therefore, the attention of many researchers is drawn to measuring the orbital angular momentum (OAM) of vortex beams [7, 21–30] that is directly related to the spectrum of optical vortices. Really, the complex amplitude $\Psi(x,y,z)$ of a composite paraxial beam can be written in the form of a superposition of the orthogonal vortex modes $\psi_m(x,y,z)$

$$\Psi(x,y,z) = \sum_{m=-N}^{N} C_m \Psi_m(x.y,z), \tag{1}$$

where $C_m = \langle \Psi | \psi_m \rangle$ stands for the mode amplitudes specified by the normalizing condition $\sum_{m=-N}^{N} |C_m|^2 = 1$, and $2N$ is a total number of vortex modes, Then the average on photon OAM of the composite beam is found by the formula [31].

$$\ell_z = \sum_{m=-N}^{N} m\,|C_m|^2. \tag{2}$$

The basis of this expression is an implicit connection between the topological charge m and the OAM ℓ_{zm} of a single mode in the beam. However, expression (2) includes the squared modulus $|C_m|^2$ of a complex number while we are talking about measuring the complex number C_m itself, i.e., its amplitude and the initial phase. The known for us approaches to measuring OAM sorting modes can be divided into four groups according to the methods used. All known for us approaches to measuring OAM spectrum and mode sorting can be conditionally divided into four groups according to the methods used and the effect on the internal beam structure. The most widely used method of holographic spatial filtering of the Laguerre-Gaussian, Hermite-Gaussian, Bessel-Gaussian, Airy-Gaussian and other mode types [22–24, 30]. At that, this method allows modes sorting, both by topological charge (azimuthal numbers m) and by radial numbers n. The holographic mode sorting resembles the effect of a "white light" decomposition into a color spectrum by means of a prism or diffraction grating. The second type of measurements requires the use of a so-called log-polar transparency and diaphragms [6, 7, 24] placed along the path of a complex beam. Such a structured transparency converts the beam into a set of horizontal or vertical fringes, the pattern analysis of which allows one to obtain the OAM spectrum. The direct application of digital processing of interference patterns of a composite vortex beam [32] and a collinear phase-shifting holography [33] can be considered as the third interference technique. However, measurements in the listed above approaches lead to complete or partial damage of the combined beam and losses of useful information. At the same time, an original approach presented in the papers [26, 27, 34] to measuring the OAM in the vortex beams with a fractional topological charge enables one to avoid the beam damage in the result of employing cylindrical lenses and analyzing the second order intensity moments [35]. Unfortunately, such a simple approach is not applicable for both sorting and measuring the spectrum of vortex modes. In [26, 27], the technique analyzes a fractional OAM [36]

of the combined beam as a whole at the focal plane of the cylindrical lens without cutting and gluing the wavefront while the first two techniques distorts radically the initial beam structure. In the technique [26], the measurement of second-order intensity matrix elements was used that enables the authors to devoid breaking down the beam structure. However, it makes sense to use such an approach only if the modes of a complex beam have axial symmetry. The authors of [34] improved the technique by using two cylindrical lenses whose axes are rotated by the angle $\pi/2$ relative to each other. This made it possible to measure the fractional OAM for any type of the mode beam symmetry.

At the same time, the measurement of the fractional OAM does not give complete information about the combined beam content. As can be seen from expression (2), the same value of the OAM can correspond to a different composition of vortex modes with squared amplitudes C_m^2. For example, in a weakly turbulent medium [37] or optical fibers [38], there is an intense energy exchange between the vortex modes of the singular beam. It makes to change both the magnitude and the spectrum of the vortex modes including their initial phases. To measure the vortex spectrum, a special technique was developed based on the analysis of higher-order intensity moments [25] at the focal plane of a spherical lens. A characteristic feature of this technique is the ability to measure not only amplitudes but also the initial phases of the vortex modes. The point is that the intensity moments at the focal plane of the spherical lens are degenerate with respect to the sign of the vortex topological charge. Therefore, the authors of [25] note that the technique is applicable only for nondegenerate spectra of combined singular beams. In [39], the authors expanded the possibilities of measuring the vortex spectrum, also covering optical vortices with different signs of topological charges due to additional transformations of the Laguerre-Gauss beams (LG) into Hermite-Gauss ones (HG) via astigmatic conversions at a cylindrical lens [40]. However, the method of measuring optical vortices in LG beams of higher orders remained uncovered.

In this chapter, we consider in detail the technique of measuring the vortex spectrum based on the analysis of high-order intensity moments that excludes cuts and gluing of the beam without losses of information on initial mode phases. Unlike the method of holographic gratings that transforms a combined beam into vortex modes with different propagation directions, just as a prism converts "white" light into a spatial frequency spectrum, we will try to demonstrate how a perturbed singular beam can be sorted into vortex modes sited in computer memory cells and then reproduce the beam main characteristics: OAM, information entropy, and initial topological charge in real time. Moreover, knowing the digital spectrum, the beam can be recovered again, and by adjusting the spectral vortex amplitudes we can improve the structure of the transmitted field.

2. Preliminary remarks

As far as we know, the first theoretical and experimental studies of optical vortex arrays refer to 1991, when the authors of [41] succeeded in reproducing holographically individual letters and words due to ordering optical vortex array in typical phase skeleton on the base of the technique that had been developed back in the early 1980s [29]. However, only after the article [42] by Berry did the studies of the vortex array properties become widespread. As a result, it was shown that the diffracted beam turns into a combined beam containing a large number of optical vortices with integer topological charges. These are sometimes called the beams with fractional topological charges. Using Eq. (2), we can verify that beams with a fractional topological charge also have fractional OAM ℓ_z. However, in the process

of shaping such beams, Eq. (2) requires careful use. Indeed, it is assumed that the functions Ψ_m of mode beams in Eq. (2) are normalized; otherwise, misunderstandings arise. For example, in [43] considers a Bessel beam diffracted by a holographic grating with a fractional topological charge (see the callout in **Figure 1**).

If the Bessel beam is represented in the form of a conical beam of plane waves with fractional phase bypath p, then after the inverse Fourier transform we get the non-normalized superposition of Bessel-Gauss modes, including vortices with both positive and negative topological charges:

$$\Psi = 2NGe^{ip\pi}\sin(p\pi)\sum_{m=-\infty}^{\infty} i^m J_m(KR)e^{im\varphi}/(p-m), \tag{3}$$

where $J_m(x)$ stands for a Bessel function of the first kind and m order, $R = r/w_0$, r and φ are polar coordinates, $N = \exp\left(iK^2/2kZ\right), G = \exp\left(ikr^2/2Z\right), Z = z - iz_0$, w_0 is a beam waist at $z = 0$, K is a scale parameter, k is a wavenumber. After the corresponding transformations, we find the OAM of the perturbed beam

$$\ell_z = \sum_{m=-\infty}^{\infty} mI_m\left(|K|^2w_0^2/4\right)/(p-m)^2 / \sum_{m=-\infty}^{\infty} I_m\left(|K|^2w_0^2/4\right)/(p-m)^2. \tag{4}$$

The result of the plotting is represented by the curve 1 in **Figure 1(a)**. The OAM oscillates at large values of the topological charge p. The integer values of the topological charge p correspond to sharp bursts of the OAM ℓ_z. However, a small deviation of the parameter p from the integer value causes sharp OAM dips. A completely different situation occurs if the elementary beams in Eq. (3) are normalized, as the authors of [44] do, the OAM oscillations disappear (see **Figure 1(b)** and curve 2 in **Figure 1(c)**). In this case, OAM $\ell_z(p)$ obeys a simple relation (see also [45])

$$\ell_z = p - \sin(2\pi p)/\pi. \tag{5}$$

The OAM oscillations disappear (see **Figure 1(c)**, curve 2). As the authors of [45] revealed, a gradual increase in OAM is observed only at small values of the fractional topological charge. In fact, we are dealing with different beams, although the basis for their shaping is the same physical process. As we will see later, the

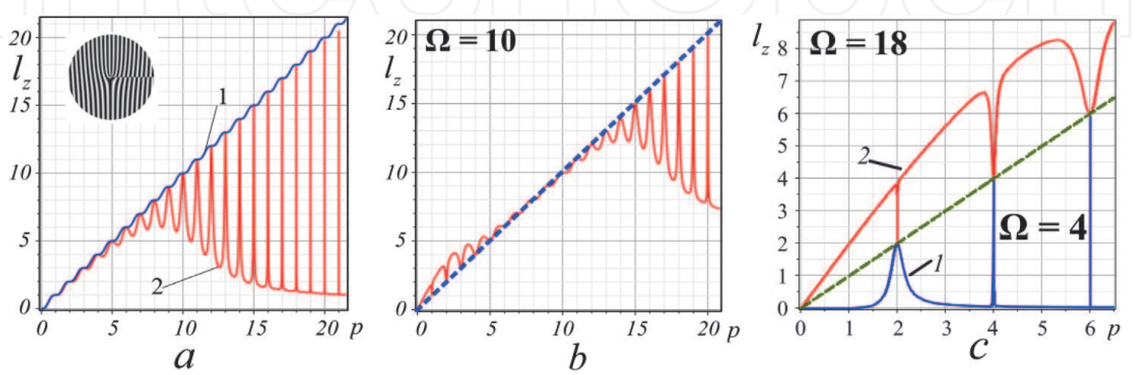

Figure 1.
(a) Dependence of the OAM ℓ_z on the fractional topological charge p*: curve 1 is calculated according to Eq. (3) with $K = 2 \cdot 10^4 m^{-1}$, curve 2 presents Eq. (5), leader—diffraction grating for $p = 5/2$. (b and c) Computer modeling of the OAM curves $\ell_z(m)$ related with combined beams in Eq. (4): (b) total value of the OAM curves at $\Omega = 10$; (c) the characteristic spectral bursts of OAM; curve 1—the OAM bursts ($\Omega = 0.4$), curve 2—dips of the OAM ($\Omega = 14$).*

choice of the normalization of vortex modes endows the combined beam with special properties.

3. Theoretical background of the digital vortex sorting and experimental results

3.1 Nondegenerate case

For a simplest model for our studies, we choose a scalar field of wave in the form of superposition LG_n^m of the lowest order with the N monochromatic beams, where $m > 0$ and $n = 0$ are the azimuthal and radial indices, respectively, so that all the vortex modes in superposition have the same waist radius w_0 at $z = 0$. Let us consider the wave field in the waist plane $z = 0$ in the form [25].

$$\Psi(r, \varphi, z = 0) = \sum_{m=0}^{N-1} C_m LG_{n=0}^m = \sum_{m=0}^{N-1} C_m r^m e^{i(m\varphi+\beta_m)} G(r, z)/N_m, \tag{6}$$

where $N_m = \sqrt{2^{-m-1} m! \pi}$ stands for the normalization factor, C_m is the mode amplitude, β_m is the initial mode phase. We consider the nondegenerate case of the field representation($m \geq 0$ or$m \leq 0$) due to the axial symmetry; combined beams with different topological signs $\pm m$ are indistinguishable in intensity moments.

Our goal is to analyze the distribution of the wave field intensity $\Im(r, \varphi, z = 0)$ in such a way as to express the squared amplitudes and the initial phases of the vortex modes in terms of physically measured quantities in the region of the beam waist. For this, we make use of the intensity moments approach [35] in the form

$$J_{p,q} = \iint_S M_{p,q}(r, \varphi) \Im(r, \varphi) r\, dr\, d\varphi / \iint_S \Im(r, \varphi) r\, dr\, d\varphi, \tag{7}$$

where the intensity distribution is written as

$$\Im = \Psi^* \Psi = \sum_{m=0}^{N-1} \frac{C_m^2}{N_m^2} r^{2m} G(r)^2 + 2 \sum_{\substack{m, m'=0, \\ m > m'}}^{N-1} \frac{C_{m'} C_m}{N_m N_{m'}} r^{m+m'} \cos\left[(m - m')\varphi\right] \cos \beta_{m,m'} G(r)^2$$

$$-2 \sum_{\substack{m, m'=0, \\ m > m'}}^{N-1} \frac{C_{m'} C_m}{N_m N_{m'}} r^{m+m'} \sin\left[(m - m')\varphi\right] \sin \beta_{m,m'} G(r)^2, \tag{8}$$

$M_{p,q}(r, \varphi)$ stands for the intensity moments function, $p, q = 0, 1, 2, \ldots$. Now the problem is to choose a combination of intensity moments $J_{p,q}$ in such a way as to exclude all terms of the last two sums and leave only the first one in Eq. (7). The equations for the squared amplitudes and the initial phases are separated if the moment function is written as $M_p(r, \varphi) = r^p$. Then the equations for the squared amplitudes take the form

$$\sum_{m=0}^{N-1}\frac{(N-1+m)!}{m!}C_m^2=\sum_{j=0}^{p}\binom{p}{j}J_{2j,2(p-j)},p\le N-2,$$
$$\sum_{m=0}^{N-1}\frac{m+1/2}{4\sqrt{2}m!}\Gamma(m+1/2)\,C_m^2=\sqrt{J_{2,0}+J_{0,2}}. \tag{9}$$

The right-hand sides of the linear Eq. (9) are easy to calculate, and the left-hand sides are directly measured experimentally using the Eq. (7) that gives the desired values of the squared amplitudes C_m^2.

As intensity of array of the beams depends only on the difference of phase between two pairs of modes, in computation of the initial phases we will assume that one of beams phase is given (let us say $\beta_0=0$). Now it is important to select the combination of moments of intensity $J_{p,q}$ that so either the second or the third sum in Eq. (2) is considered in the calculation. It is natural to calculate not all differences of phase $\beta_{m,m'}$, but only $\beta_{0,m}$. However, we did not find such combinations $J_{p,q}$ that could filter out only terms with $\beta_{0,m}$. Generally speaking, to calculate the phase difference $\beta_{m,m'}$ it is required to find the M equations for variables $X_{m,m'}=C_mC_{m'}\cos\beta_{m\,m'}$ and $Y_{m,m'}=C_mC_{m'}\sin\beta_{m,m'}$ in Eq. (2) the second and third sum, number of which is equal to the number of 2-combinations of N elements. It turns out that the number of equations can be significantly decreased if using the moments $J_{2(p+1),1}$ for $X_{m,m'}$ variables and $J_{1,2(p+1)}$ for $Y_{m.m'}$ variables. The system of linear equations for the phase difference are written in the form

$$J_{2(p+1),1}=\frac{1}{2^{2(p+1)}}\sum_{m=0,}^{N-1}\sum_{k=0}^{p}\binom{2p}{k}\left[\frac{M_{m,n_1}}{N_nN_{n_1}}X_{m,n_1}+\frac{M_{m,n_2}}{N_mN_{n_2}}X_{m,n_2}\right], \tag{10}$$

$$J_{1,2(p+1)}=\frac{1}{2^{2(p+1)}}\sum_{m=0,}^{N-1}\sum_{k=0}^{p}(-1)^{p-k}\binom{2p}{k}\left[\frac{M_{m,n_1}}{N_mN_{n_1}}Y_{m,n_1}+\frac{M_{m,n_2}}{N_mN_{n_2}}Y_{m,n_2}\right]. \tag{11}$$

where $n_1=|m-2(p-k)\pm3|, n_2=|m-2(p-k)\pm1|, M_{m,n_{1,2}}=\int_0^\infty r^{m+n_{1,2}+1}G^2dr$. The number of linear equations in each system Eqs. (10) and (11) is $K=3(N-3),\ \ N\ge6$. It is noteworthy that Eqs. (10) and (11) contain only the terms with an odd difference of indices, including $\beta_{0,m}$, so that a finite solution enables us to obtain all phases of the partial beams in the form $\tan\beta_{m,m'}=Y_{m,m'}/X_{m,m'}$.

A key element of the experimental setup in **Figure 2(a)** was a spatial light modulator SLM (Thorlabs EXULUS-4K1), which converted the fundamental TEM_{00} mode of the He-Ne laser (wavelength $\lambda=0.6328\,mcm$ and power 1 mW) into a composite beam with mode amplitudes C_m and initial phases β_m. To make this possible, the laser beam was additionally filtered by the system FF. The beam splitter BS formed two working arms of the experimental setup. The beam in the first arm projected by a spherical lens onto the input pupil of the CCD1 camera (Thorlabs DCC1645) is subjected to the image computer processing. The result of the computer processing is a digitization of the beam intensity distribution and calculations of high-order intensity moments J_{pq}. Additional computer software made it possible to compose a system of linear Eqs. (9)–(11) and calculate both the mode amplitudes C_m and their initial phases β_m in real time. The second arm was in use for the control measurement of the OAM of the composite beam. For this purpose, the beam was focused by a cylindrical lens CL onto the input pupil of the

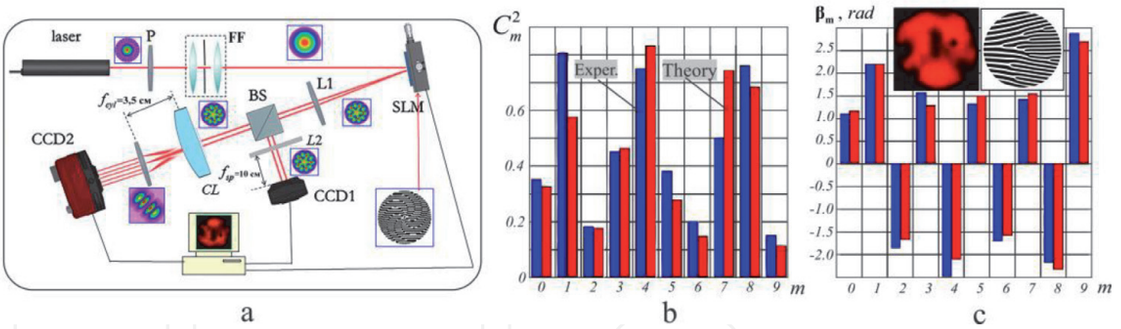

Figure 2.
(a) Model of experimental setup for real-time vortex measurement and value of the OAM, P—polarizer, FF—light filter of space, SLM—space light modulator, L1, L2—spherical lenses with focal length f_{sh}, BS—beam splitter, CL—cylindrical lens with a focal length f_{cyl}, CCD1,2—CCD-color cameras; (b and c) the vortex spectrum of the beam array with $N = 10$: (b) $C_m^2(\mathrm{m})$, (c) $\beta_m(\mathrm{m})$ the OAM: theory $\ell_z = 0.39$, experiment $\ell_z = 0.42$; callout: the intensity distribution and corresponding diffraction grating.

second CCD2 camera (Thorlabs DCC1645) then the second-order intensity moment J_{xy} was measured and the average OAM per photon was calculated in accordance with the technique described in detail in the paper [26].

Before proceeding to the current measurements, it was necessary to adjust the experimental setup. For this, a number of calibration measurements were carried out. The digitization of the intensity distribution $\Im(x,y)$ required normalization of the transverse coordinates x,y in units of the Gaussian beam waist at the plane of the CCD camera. To measure the initial beam waist radius w_0, the second-order intensity moments J_{12} were used in accordance with the beam quality measurement method [46]. In order to ensure calibration measurements, a special computer program was developed that assigned random values of the amplitudes and initial phases of the vortex modes in Eq. (1) due to the random-number generator. Then, an appropriate diffraction grating was formed on the liquid crystal element of the SLM modulator and the calibration beam was restored. A typical intensity distribution of the calibration beam is shown in the callout of **Figure 2(c)**. The corresponding spectra of the squared amplitudes $|C_m|^2$ and initial phases β_m are presented in **Figure 2(b)** and **(c)**. Red and blue colors in **Figure 2(a)** and **(b)** present experimental and theoretical data, respectively. Note that the OAM measured in the second arm was $\ell_z = 4.2$ and the first arm calculated according to Eq. (2) was $\ell_z = 4.5$, while the theory gives $\ell_z = 4.9$. The measurement error for $N = 10$ beams did not exceed 3–4% for amplitudes and 5–6% for phases. The most interesting effect is observed in the region of OAM oscillations in **Figure 1(a)** with a characteristic perturbation of the holographic grating in **Figure 2(c)**. This effect is accompanied by a sharp restructuring of the vortex spectrum. For small perturbations of the singular beam, additional vortex modes arise only near the initial value of the topological charge $m = M$ (see [47]). However, in general case of the hologram perturbation, vortex modes with opposite signs of topological charges appear. Such a vortex spectrum reconstruction cannot be detected using the above approach. It is required to expand the measurement technique.

3.2 Degenerate case and vortex avalanche

We consider the case when the initial LG beam with a zero radial index $n = 0, m \neq 0$ is subjected to local perturbation at the central region of the holographic grating. As a result of the perturbation, vortex modes with various types of topological charges appear in the beam. The method of the beam expansion in a series over the vortex modes depends on the type of the grating perturbation. We suppose

(and then prove) that the chosen perturbation does not excite LG modes with radial indices $n = 0$, but only modes with different topological charges m appear [39]. Then we write the complex amplitude of the perturbed beam in the form

$$\Psi(R,\varphi,z) = \sum_{m=-N}^{N} \frac{C_m R^{|m|} e^{i\,m\,\varphi} G(R)}{M_m \sigma^{|m|+1}(z)}, \tag{12}$$

where M_m is a normalized factor and $\sigma(z) = 1 - iz/z_0$.

It is important to notice the intensity moments $J_{p.q}$ are degenerate with respect to the sign of the vortex topological charge m in the case of axial symmetry of the modes in Eq. (12). To remove degeneracy of the intensity moments, it is important to change symmetry of singular beams, but without destroying of structure beams so that the vortex modes with opposite topological charges in sign have distinct geometric contours. Such a requirement provides by the astigmatic transformation with a cylindrical lens of the Laguerre-Gauss beam, which was considered detail in [34] (the general theory of paraxial astigmatic transformations can be found in [41]). We suppose that the cylindrical lens with a focal length f is located at the plane $z = 0$. A paraxial beam with complex amplitude (12) is projected at the lens input. The plane of the beam waist is matched with the plane of the lens. Besides, we restrict our study to zero initial phases of mode beams, i.e., amplitudes C_m are real values. Then, following [34], we write the complex amplitude of a combined beam at the wave diffraction zone as

$$\Psi_{CL}(x,y,z) = \sum_{m=-N}^{N} A_m H_m(F)\,\exp(\Phi), \tag{13}$$

where $A_m = -i\frac{z_0}{z}\frac{1}{qq_0}\left(-\frac{w_0}{q_0}\right)^m\left(1-\frac{q_0^2}{q^2}\right)$, $\Phi = i\frac{k}{2z}(x^2+y^2) - \left(\frac{z_0}{zw_0q}\right)^2 x^2 - \left(\frac{z_0}{zw_0q_0}\right)^2 y^2$, $F = \frac{z_0}{w_0 z}\frac{i\frac{q_0}{q}x - \frac{q}{q_0}y}{\sqrt{q^2-q_0^2}}$, $q_0^2 = 1 - i\frac{z_0}{z}, q^2 = 1 + i\frac{z_0}{z_1}, z_1 = \frac{zf}{z-f}$..

Let us consider new normalized coordinates so that the beam axes are directed by an angle $\pi/4$ relative to the axes of the cylindrical lens: $u = (x+y)/w_0, v = (x-y)/w_0$, we will consider field of paraxial beam in double focus plane $z = 2f$, and also require that $z_0/2f = 1$. Then distribution of the beam intensity is written as

$$\Im = |\Psi_{CL}|^2 = \left\{ \sum_{m,n=0}^{N} C_{-n}C_{-m}\frac{A_{m,n}}{N_{m,n}} H_n\left(\frac{u}{\sqrt{2}}\right)H_m\left(\frac{u}{\sqrt{2}}\right) + \sum_{m,n=1}^{N} C_n C_m \frac{A_{m,n}}{N_{m,n}} H_n\left(\frac{v}{\sqrt{2}}\right)H_m\left(\frac{v}{\sqrt{2}}\right) \right.$$
$$\left. + \sum_{\substack{n=0,\\ m=1}}^{N} C_{-n}C_m\frac{A_{m,n}}{N_{m,n}} H_n\left(\frac{u}{\sqrt{2}}\right)H_m\left(\frac{v}{\sqrt{2}}\right) + \sum_{\substack{n=1,\\ m=0}}^{N} C_n C_{-m}\frac{A_{m,n}}{N_{m,n}} H_n\left(\frac{v}{\sqrt{2}}\right)H_m\left(\frac{u}{\sqrt{2}}\right) \right\} \exp\left(-\frac{u^2+v^2}{2}\right) \tag{14}$$

where $H_n(x)$ is Hermite polynomials, $A_{m,n} = (-1)^{|n|+|m|}e^{i\frac{|m|-|n|}{4}\pi}$, $N_{n,m}^2 = \frac{\pi}{4}\left(\frac{w_o}{2}\right)^{n+m} 2^{n+m+1} n!m!$. As can be seen from Eq. (14), the terms corresponding to optical vortices with positive and negative topological charges are only partially divided. The last two terms characterize the cross terms $C_{-n}C_m$ and C_nC_{-m}. Besides, the first two terms also contain cross amplitudes $C_{-n}C_{-m}$ and $C_nC_m(|n| \neq |m|)$. On the other hand, our task is to measure only the squared amplitudes C_m^2. It is important to note, that the factors $A_{m,n} = -A_{n,m} = i$ with the difference of the

indices $|m-n|=2$ in Eq. (14) are imaginary, therefore the cross terms of the beam intensity distribution with such indices difference disappear.

It seems that for solving this problem it is reasonable to choose intensity moment functions in the form of Hermite polynomials Eq. (14) as $M_{p,0}(u)=H_p\left(u/\sqrt{2}\right)$ and $M_{0,q}(v)=H_q\left(v/\sqrt{2}\right)$. Next, one can use the orthogonality condition of the HG beams and write a system of linear equations, the number of which is equal to the number of variables, as was done above for a non-degenerate vortex array. However, as shown by the assessed computations, as the indices p and q increase along with the $2N$ variables C_m^2, the $2N-6$ cross terms $C_{\pm n}C_{\pm m}$ and $C_{\pm n}C_{\mp m}$ are also added. The system of Eq. (14) cannot be closed. However, one can act otherwise. First, we make two Fourier transforms of the intensity distribution $\Im(x,y)$ in the form

$$\Im(\xi)=\int_{-\infty}^{\infty}\int_{-\infty}^{\infty}\cos\left(\xi\frac{u}{\sqrt{2}}\right)\Im(x.y)\,dx\,dy,\quad \Im(\eta)=\int_{-\infty}^{\infty}\int_{-\infty}^{\infty}\cos\left(\eta\frac{v}{\sqrt{2}}\right)\Im(x.y)\,dx\,dy. \tag{15}$$

In particular, the terms $\Im_{-m.-n}$ in the intensity distribution $\Im$ are

$$\begin{aligned}\Im_{-m.-n}(\xi)=\int_{-\infty}^{\infty}\int_{-\infty}^{\infty}\cos\left(\xi\frac{u}{\sqrt{2}}\right)\Im(x.y)\,dx\,dy=\sum_{n=0}^{N}C_{-n}^2\frac{2^{n+1/2}}{N_{n,n}}\xi^{2n}L_n\left(\frac{\xi^2}{2}\right)e^{-\frac{\xi^2}{4}}\\ +\sum_{\substack{m,n=0,\\ |m-n|\neq 0,2}}^{N}C_{-n}C_{-(n+2m)}\frac{(-1)^{n+2m}2^{n+1/2}}{N_{m,n}}\xi^{2m}L_n^{2m}\left(\frac{\xi^2}{2}\right)e^{-\frac{\xi^2}{4}},\end{aligned} \tag{16}$$

Thus, after the Fourier transform the distribution of intensity $\Im(\xi,\eta)$ contains all the squared amplitudes, and, also, the cross terms with the difference $|m|-|n|=\pm 4$. The cross terms $\Im_{-m,m}$ and $\Im_{m,-n}$ refer to vortices with positive and negative charges. Besides, the terms $\Im_{-m,-(n+2m)}(\xi)$ includes amplitudes C_{-n}^2 with the similar coefficients, and the member $\Im_{m,(n+2m)}(\xi)$ includes amplitudes C_n^2 with only different coefficients. The expressions are received for the terms, that $\Im_{-m,-(n+2m)}(\eta)$ and $\Im_{m,(n+2m)}(\eta)$, if we swap the signs of the indices.

The equations for squared amplitudes $C_{\pm n}^2$ will be found, if we will make use the full basis of the Laguerre-Gaussian modes for expansion of the intensity moments:

$$J_{p,2q}^{(+)}=\int_{-\infty}^{\infty}\xi L_p^{2q}\left(\frac{\xi^2}{2}\right)\Im(\xi)\,d\xi/J_{00},\quad J_{p,2q}^{(-)}=\int_{-\infty}^{\infty}\eta L_p^{2q}\left(\frac{\eta^2}{2}\right)\Im(\eta)\,d\eta/J_{00}, \tag{17}$$

where J_{00} is a total beam intensity and $L_p^q(x)$ is Laguerre polynomials. Then, using [39], we find a system of linear equations

$$J_{p,q}^{\mp}=\left(\sum_{n=1}^{N}C_{\mp n}^2+\frac{(2q+p)!(1/2)^p}{p!4^{-(2q+p+1)}}\sum_{m,n=1}^{N}\frac{(2m+n)!(1/2)^n}{n!4^{-(2m+n+1)}N_{nm}}\,C_{\pm n}C_{\mp m}\right)/J_{00}, \tag{18}$$

The system of Eq. (18) enables us to find the values of the squared amplitudes via the measured values of the intensity moments $J_{p,q}^{\pm}$. Each equation contains $2N$ terms for amplitudes C_m^2 and $N-3$ cross terms C_mC_n. Increasing the value of the

indices p and q does not change the number of variables, so the system of Eq. (18) can be closed. Note that each of the Eq. (18) can be solved independently of each other and find the amplitudes C_m^2 and C_{-m}^2. The total number of linear equations is relative to signs $(\pm)$, so that the systems can be easy solved for finding the squared amplitudes in real time using modern computer software.

For measurements, the experimental setup shown in **Figure 2(a)** was used. However, in contrast to the non-degenerate case, the main experimental data were measured in the second arm, provided that the detection plane was located at the double focus region of the cylindrical lens, while the first arm was used for general adjustment [39].

We will implement the above technique for a new type of combined beams with conspicuous dips and bursts in the OAM spectrum similar to that shown in **Figure 1(a)** and **(b)**. Let us write the complex amplitude of the combined vortex beam in the form

$$\Psi(r,\varphi,z) = \sin(p\pi)e^{iP\pi}\sum_{m=-N}^{N}\begin{pmatrix}\cos(m\pi/2)\\ \sin(m\pi/2)\end{pmatrix}\frac{\Omega^{|m|}}{|m|!(M-m+\delta p)}\frac{R^{|m|}e^{im\varphi}}{\sigma(z)^{|m|+1}}\exp\left(-R^2\right), \tag{19}$$

where Ω is a scale parameter, δp stands for the perturbation of the holographic grating responsible for shaping the beam, M is a topological charge of the non-perturbed forked grating. Factors $\cos(m\pi/2)$ or $\sin(m\pi/2)$ thin out the vortex spectrum remaining the modes with either even or odd $m-$ indices. This makes the dips in the OAM spectrum more distinct. The complex amplitude (12) corresponds to the OAM in the form

$$\ell_z = \sum_{m=-N}^{N} m\begin{pmatrix}\cos^2(m\pi/2)\\ \sin^2(m\pi/2)\end{pmatrix}\frac{\Omega^{2|m|}}{|m|!^2(M-m+\delta p)^2}\Big/\sum_{m=-N}^{N}\begin{pmatrix}\cos^2(m\pi/2)\\ \sin^2(m\pi/2)\end{pmatrix}\frac{\Omega^{2|m|}}{|m|!^2(M-m+\delta p)^2}. \tag{20}$$

Figure 1(b) and **(c)** displays the case of even vortices beams in the curves of $\ell_z(p)$. The spectrum of OAM in **Figure 1(b)** characterizes the general view of resonant bursts and dips. The Ω parameter of scale admits displace along the axis of the resonant regions $p = M + \delta p$. **Figure 1(c)** (curves 1 and 2) describes their characteristic features. In the even vortex modes of integer topological charge are located resonant dips. Swaps of the cosine with the sine in Eq. (19) displaces along the axis p of the resonant regions by one. Increase of the topological charge M is accompanied by resonances compression, until their depth gets become approximately equal to M at $\Omega = 18$ and $p < 6$. For large parameters $\Omega >> 20$, the OAM is doubled $\ell_z = 2M$ in range of the initial topological charges M. As was shown in [47, 48], a perturbation δp causes a local distortion of the forked grating defect for the large values parameter p shown in **Figure 3(a)**.

As the perturbation grows the area of the hologram defect increases (**Figure 3(b)**). Small variations in the holographic grating structure lead to a cardinal reconstruction of the vortex spectrum (**Figure 4(a)**). Weak perturbations $\delta p \sim 10^{-2}$ of the grating cause an avalanche of optical vortices. The satellites appear in the OAM spectrum, the maxima of which has topological charges less than the initial M. The energy of the basic mode M flows partially into the spectral satellites, that are generated both in the region of positive $m > 0$ and negative $m > 0$ topological charges.

For large perturbations $\delta p \sim 0.1$, a vortex avalanche picks almost all the energy out of the basic mode. The vortex avalanche at small deviations δp of the topological

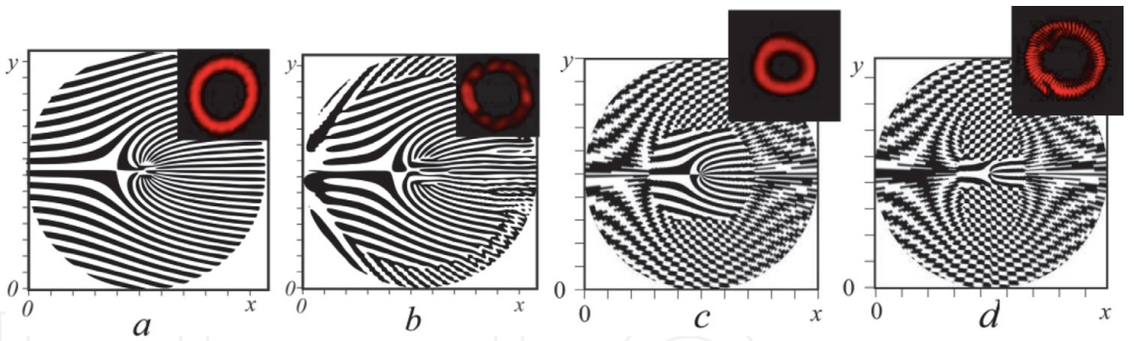

Figure 3.
Forked defect perturbations of the holographic gratings with (a and b) $M = 20$, $\Omega = 2.1$, (c and d) $M = 4$, $\Omega = 14$: (a) $\delta p = 10^{-3}$, (b) $\delta p = 0.1$, (c) $\delta p = -10^{-3}$ (d) $\delta p = -0.5$, callouts: intensity distributions of the beams restored by the perturbed holograms.

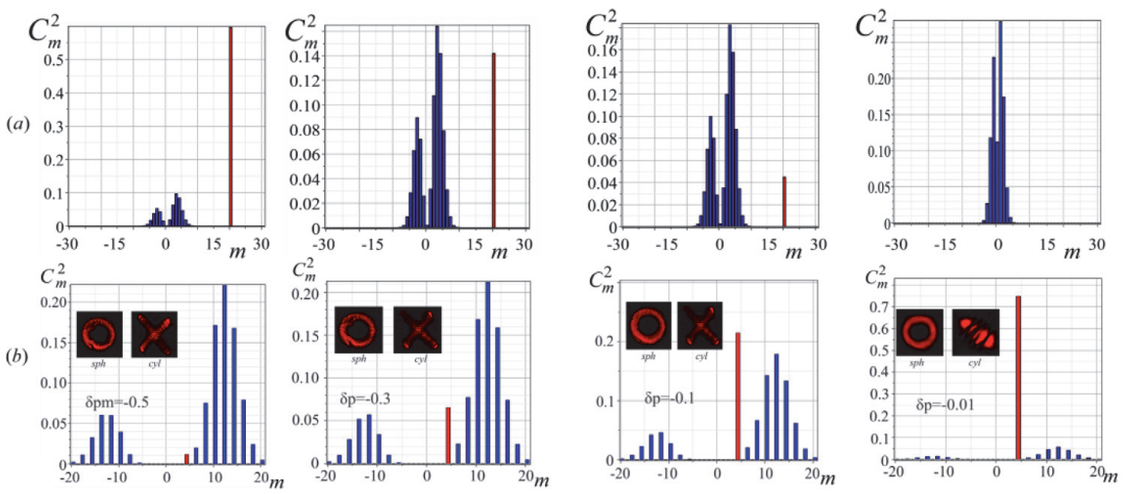

Figure 4.
Experimental vortex spectra $C_m^2(m)$ for perturbed singular beams with (a) $M = 20$, $\Omega = 3.5$ and (b) $\Omega = 18, M = 4$; callouts: intensity distributions at the beam waist after spherical (sph) with focal length $f = 0.1$ m and cylindrical (cyl) lens with $f_{cyl} = 0.5$ m; red color—an initial mode.

charge from integer values M immediately causes a resonance dip in the OAM spectrum (**Figure 5(a)**). With increasing M the depth of the dip decreases while its shape is distorted (see **Figure 5(b)**).

Absolutely other situation arises when the holographic grating with $M > 10$ and a forked defect is subjected to a small perturbation. As shown in **Figure 3(c)**, even a weak perturbation $\delta p = -0.001$ changes drastically the entire relief of the holographic grating although the intensity distribution. In the result, even small differences in the grating relief affects inevitably the shape of the vortex spectrum

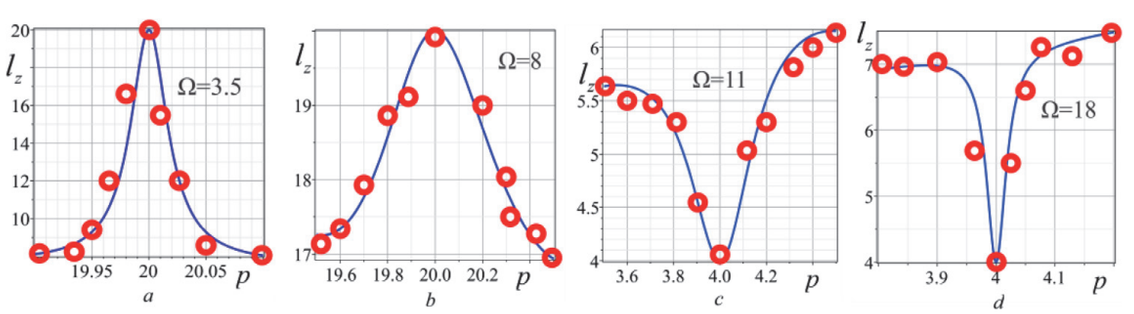

Figure 5.
Dips and bursts in the OAM spectrum $\ell_z(p)$ at various beam parameters Ω and M, $p = M + \delta p$: (a and b) $M = 20$, (c and d) $M = 4$; solid lines—theory, circles—experiment.

$|C_m(m)|^2$ and $\Omega > 10$ induce the vortex avalanche (see **Figure 4(b)**). However, the avalanche type differs significantly from that in the previous case. Indeed, as well as in the above case, the perturbation provokes appearing resonance satellites with both positive and negative topological charges (TC). However, their values are always greater than those of the initial TC. In this case, energy is also pumped from the basic mode to the satellites but with higher topological charges under the condition of the resonance $m = p$. In the OAM spectrum, it looks like the OAM burst at the resonance as shown in **Figure 5(c)** and **(d)** but the maxima ℓ_z are at the region of fractional values p. As the scale parameter increases, the height of the flash decreases, and the resonance circuit broadens (**Figure 5(d)**).

Further increasing the parameter p ($\Omega = const$) is accompanied by smoothing the curve $\ell_z(p)$ so that $\ell_z|_{\max} \to 2p$ except for the OAM dips at the integer values $m = p$.

4. OAM, informational entropy and topological charge of truncated vortex beams

A special case is represented by natural changes of the vortex spectrum due to external influences on the laser beam (diffraction by opaque obstacles, external interference in the beam, etc.). The simplest opaque obstacles are the sector, circular and annular apertures where we stop our attention using a simple technique of the vortex digital sorting.

4.1 Sector aperture

Let us consider propagation a scalar beam of Laguerre-Gaussian LG_0^m with a zero radial index $p = 0$ and an azimuthal index (a topological charge) m through the rough regular sector aperture obstacle, that an angle shown in **Figure 1**. The edge of sector touches axis of the beam. The field of beam at the initial plane $z = 0$ can be represented as [49].

$$\Psi_m(r, \varphi, \alpha) = (\rho/w)^{|m|} e^{i m \varphi} e^{-\rho^2/w^2} = r^{|m|} e^{i m \varphi} e^{-r^2}, \quad \alpha < \varphi < 2\pi - \alpha, \tag{21}$$

where $r = \rho/w$. w is a beam waist radius at the plane $z = 0$, ρ and φ represent polar coordinates. We rewrite the beam field (1) formed by the rigid-edges aperture with the half angle α as a sum of non-normalized Laguerre-Gauss beams LG_p^m in the form

$$\Psi_m(r, \varphi, \alpha) = \sum_{n=-\infty}^{\infty} C_{m,n}(\alpha) LG_0^n(r, \varphi) = \sum_{n=-\infty}^{\infty} C_{m,n}(\alpha) r^{|n|} e^{i n \varphi} e^{-r^2}, \tag{22}$$

where the beam amplitudes are

$$C_{m,n}(\alpha) = (-1)^{m-n} \Gamma\left(\frac{|m| + |n|}{2} + 1\right) \frac{\sin\left[(m-n)(\pi - \alpha)\right]}{m - n} \Big/ \left(\pi 2^{\frac{|m|-|n|}{2}} |n|!\right), \tag{23}$$

where $\Gamma(x)$ is a Gamma function. The terms in the series (23) with radial indices $p \neq 0$ disappear due to orthogonality of the LG modes.

The complex amplitude (22) can describe the spatial evolution of the perturbed beam if we replace $r \to r/\sigma$ and multiply the sum by σ where $\sigma = 1 - iz/z_0$.

Figure 6(b) and **(c)** shows a computer simulation (**Figure 6(b)**) and experiment (**Figure 6(c)**) of the intensity distribution $\Im(r, \varphi, z) = \Psi\Psi^*$ along the vortex beam length with $m = 15$ modulated by the sector aperture with $\alpha = \pi/4$. It is important to note, that the cut out dark sector from the beam intensity distribution does not lead to its self-healing. When the beam propagates, the dark sector rotates synchronously. We showed, both theoretically and experimentally, that beam self-healing does not occur at any beam length z even at a very small sector angle α.

4.1.1 The vortex spectrum

We consider vortex beams spectra for topological charge that most clearly reflect properties of the sector perturbation. Computer simulation and experimental data of typical vortex spectra is shown in **Figure 7**. We revealed a clear maximum of vortex mode intensity $C^2_{m,n}$ for the initial topological charges $n = m = 5$ with $\alpha = 45°$. The short part of the beam intensity redistributed symmetric at the neighboring vortices orders. But, if we increase the angle α, we see a violation of the symmetric distribution of intensity among the vortex modes. There formed a second maximum in the spectrum range of negative topological charges $n < 0$. It is important to note, that the authors of Ref. [50], taking into consideration the optical uncertainty principle, also plotted the vortex spectrum for a topologically neutral beam $m = 0$ and a beam with a small topological charge $m = 2$ at the angle of aperture $\alpha = 45°$. The authors did not detect a maximum of spectra in the negative region of topological charges. As we presented above, the emergence of the second

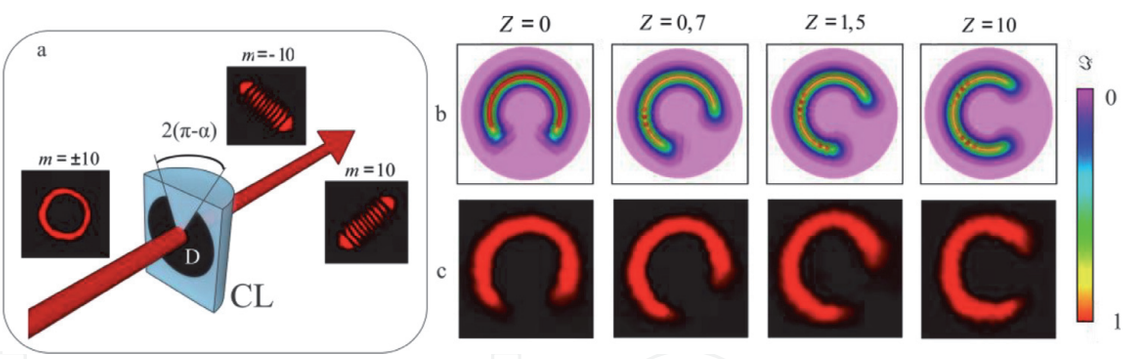

Figure 6.
(a) Sketch of the hard-edged aperture (D) installed at the cylindrical lens plane (CL). Images LG and HG beams illustrate the astigmatic transformation of a single vortex beam. (b and c) Intensity distribution $\Im(r, \varphi, z)$ of the vortex beam with $m = 15$ along length $Z = z/z_0$ perturbed by a hard-edged sector diaphragm with $\alpha = \pi/4$: (b) theory, (c) experiment.

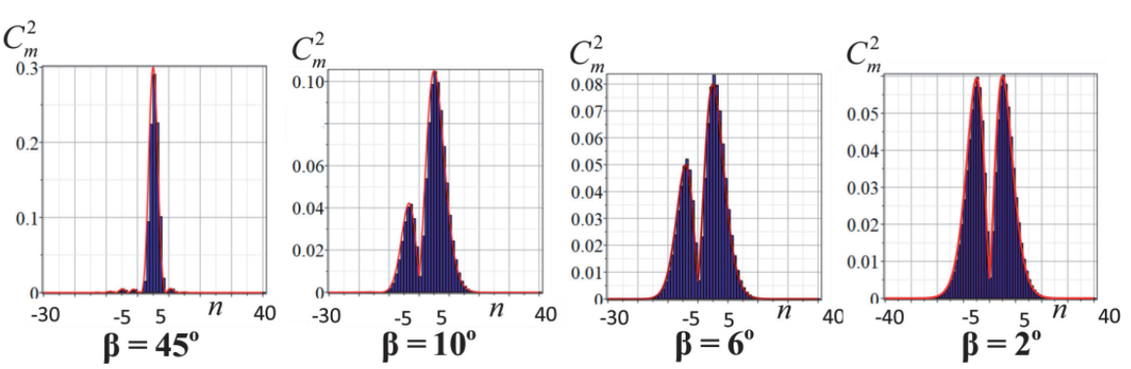

Figure 7.
Distribution of vortex beams spectrum $C^2_{m,n}$ with charges $m = 5$ perturbed by the hard-edged aperture with the sector adjacent angle $\beta = \pi - \alpha$, the solid line is spectrum outline.

intensity maximum is possible only at sufficiently large angles of overlap of beam α and also large topological charges m of the initial singular beam.

4.1.2 The orbital angular momentum

The OAM per photon of a complex perturbed beam can be calculated in accordance with Eq. (23). The mode amplitudes are given by the normalized field Ψ_m of the Laguerre-Gauss beams so that the squared amplitudes $C^2_{m,n}$ and $\overline{C}^2_{m,n}$ are obeyed a simple relation $\overline{C}^2_{m,n} = 2^{-|n|-2}|n|!C^2_{m,n}$. The changes of OAM $\ell_z(\alpha, m)$ after increasing the aperture angle α (decreasing the adjacent angle $\beta = \pi - \alpha$) is presented by **Figure 7(a)** for topological charges $m = 5, m = 10$ and $m = 15$ of the initial vortex beam.

The OAM is practically unchanged a wide range of angles and remains almost equal to the initial OAM, despite the rapid increase in the number of vortex states (see **Figure 8(a)**). After the second spectral maximum is formed in the negative region of topological charges **Figure 7**, there is a sharp decrease of the OAM. The OAM is equal to zero already at the angle $\beta \approx 2°$.

4.1.3 Informational entropy (Shannon's entropy)

The normalized squared amplitude $C^2_n \in (0, 1)$ in the Eq. (23) can be treated as a conditional probability $P(n/m)$ of finding out a vortex beam in the state $|n\rangle$ among of $2N$ states (see, e.g., [51] and references therein). This approach to counting a number of vortex states can be used for the Shannon Entropy [51] and is written as

$$H_I = -\sum_{n=0}^{N} P(n/m)\log_2 P(n/m) = -\sum_{n=0}^{N} C^2_n(\alpha, m)\log_2 C^2_n(\alpha, m) > 0. \qquad (24)$$

The Shannon entropy (24) characterizes the amount of uncertainty (randomness) that arises when a perturbation acts on a vortex beam. For example, in the case of the same amplitudes of the mode beams, the Shannon entropy of $H_I = 2$ means that to remove the uncertainty it is necessary to expend 1 bit of information.

In **Figure 8(b)** presents the dependence of the Shannon Entropy H_I on the angle α for various of number topological charges m. In a broad range of aperture angles $0 < \alpha < 7\pi/8$, the informational entropy H_I increases equally for any topological charges m while the OAM ℓ_z does not change (see **Figure 8(a)**) which corresponds to the same changes in the spectrum of vortex states in **Figure 7**.

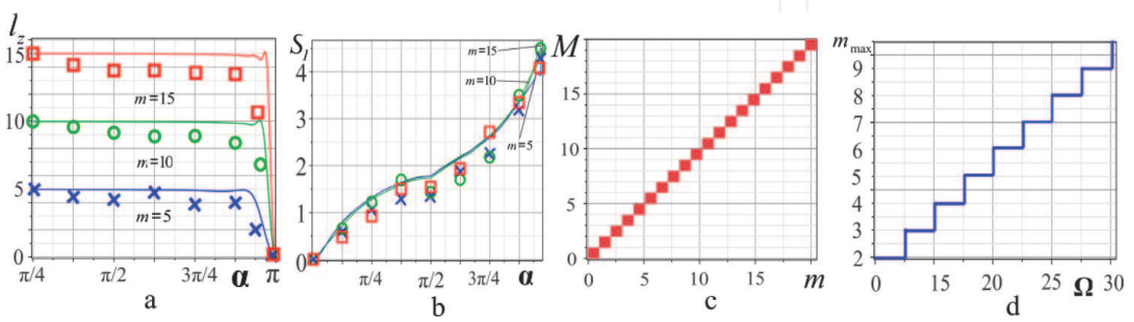

Figure 8.
Computer simulation of (a) the OAM $\ell_z(\alpha, \mathrm{m})$ and (b) information entropy $H_I(\alpha, m)$ for the initial topological charges, $m = 5, 10, 15$; (c) transformation of the vortex TC Mof the perturbed beam via variation TC of the initial beam; (d) maximal TC m_{max} of the spectral vortex satellites via perturbation Ω of the perturbed holographic gratings; (solid lines); crosslets (×), circlets (⊙) and squares (□) are correspondent experimental data.

4.1.4 The topological charge

According to Berry [42], the topological charge of the vortex array is defined as the difference of the fluxes of vortex trajectories through the beam cross section taking into account vortex directions and "weights," and is calculated as

$$M = \frac{1}{2\pi}\mathrm{Im}\left\{\lim_{r\to\infty}\int_0^{2\pi}\partial_\varphi\Psi_m/\Psi_m d\varphi\right\}. \tag{25}$$

Berry showed [42] that the vortex beam TC has always integer values when the spiral phase plate is perturbed equal to the integer value of the unperturbed plate step. We investigated the changes of the TC under the beam sector perturbations [52] and perturbation of the holographic grating [47]. Note that all further calculations are based on the requirement that the perturbation does not introduce changes in the mode phases. We performed a series of computer TC estimations of the perturbed beam (20) for various initial TC. The following restrictions were used. As the spectra of vortices in **Figure 7** show, the squared mode amplitudes quickly tend to zero as their TC increases. Therefore, we can restrict ourselves to a finite mode numbers $C_{mn}^2 \sim 10^{-3}$. The half-width beam radius can be estimated at the maximum intensity of the initial vortex beam $r_M = \sqrt{|m|/2}$. Therefore, in Eq. (25) we replaced the limit $r \to \infty$ by $r \to 3r_N$. The results of computer simulation are shown in **Figure 8(c)**. It can be seen from the figure that the total topological charge M at $\alpha = 3\pi.4$ remains equal to the initial TC of the unperturbed beam $M = m$. Computer calculations for sector aperture angles $\alpha = \pi/4, \pi/2, 30\pi/31$ show similar results. Therefore, we assume that, in the general case of arbitrary angles, the initial TC will be preserved under sector perturbations. We also examined the constancy condition TC under the perturbation of the holographic grating considered above and made sure that this condition is strictly satisfied. Moreover, we traced the maxima displacement of the spectral satellites in the vortex avalanche in **Figure 4** [47] and convinced (see **Figure 8(d)**) that their TC cannot take fractional values.

4.2 Circular and annular apertures

The problem of the birth and annihilation of phase singularities has been considered as far back as at the beginning of the last century in connection with the peculiarities of light diffraction at the edges of the half-plane or lenses and microobjectives of telescopes and microscopes (see [53] and references therein). As a rule, the discussion came down to the technique of suppressing the corresponding aberrations. In this section, we focus on the digital vortex sorting after beam diffraction by the circular and annular apertures addressing the Shannon entropy problem of the diffracted combined vortex beams.

Note also that recently, special attention has been paid to studies on increasing the information capacity of optical channels due to LG_n^m modes with various radial indices n, but a constant topological charge m [54]. Such modes are sorted using the holographic grating techniques and *a single phase screen* [55]. In this section, we will focus on the digital sorting of LG modes with various radial indices.

We consider the perturbation of the vortex LG_0^m beam at the $z = 0$ plane with a ring aperture so that its complex amplitude is written in the form (see also **Figure 10a**)

$$\Psi_m = r^{|m|}e^{im\varphi}\exp\left(-r^2\right), \quad R < r < R + h. \tag{26}$$

If the axis of the annular aperture coincides with the beam axis then the perturbation excites only LG beams with the same TC ($m = const$) but different radial indices n (this follows from the condition of orthogonally of LG beams). The perturbed beam field can be represented as an expansion over LG beams

$$\Psi_m = \sum_{n=0}^{\infty} C_{m,n} r^m L_n^m\left(2r^2\right) e^{i m\varphi} e^{-r^2}. \tag{27}$$

The LG vortex modes amplitudes restricted by the ring of thickness h, we find for the field difference the beams passing simultaneously through the circular aperture of radius $R + h$ and the opaque disk of radius R. As a result we obtain

$$\begin{aligned} C_{m,n}(R) &= \int_0^{\infty} \Psi_m \left(LG_n^m\right)^* r\, dr \\ &= \left(2(R+h)^2\right)^{m+1} e^{-2(R+h)^2} {}_1F_1\left(1-n, m+2; -2(R+h)^2\right)/(m+1)m! \\ &\quad - \left(2R^2\right)^{m+1} e^{-2R^2} {}_1F_1\left(1-n, m+2; -2R^2\right)/(m+1)m!, \end{aligned} \tag{28}$$

where ${}_1F_1$ is a confluent hypergeometric function and we used the integrals from [56]. The expression (28) together with Eq. (27) allows covering three cases: (1) a circular aperture, $R = 0, h = R_0$; (2) an opaque disk $R = R_0, h = 0$; and (3) an annular aperture $R, h \neq 0$. An important property of mode amplitudes (28) is that the perturbation of a singular beam with a defined TC via these types of axial apertures does not excite vortex modes with other TC. This means that the OAM ℓ_z does not change due to such a perturbation process. Does this mean that the perturbed vortex beam completely restores its initial properties during propagation, i.e., possesses the self-healing effect? We will peer into this process carefully.

Recall that under the action of axial perturbation, vortex modes with new topological charges do not appear in the perturbed beam. Therefore, the digital sorting of vortex modes in a perturbed beam can be carried out in accordance with Eq. (15) for the nondegenerate case (see Section 3.1). In this case, as a function of moments $M_{p,q}(r, \varphi)$ should choose the forms $M_{p,q} = \sin r L_p^k(2r^2)$ or $M_{p,q} = \cos r L_p^k(2r^2)$ while in the intensity distribution $\Im(r, \varphi)$ use the complex amplitude (26). Variation of the indices p and k enables us to obtain a closed system of linear equations for the squared amplitudes $C_{m,n}^2$.

The experimental results of measuring the vortex spectra are shown in **Figure 9**, where the average values of the squared amplitudes are plotted along the ordinate axis. A characteristic feature of the dependences $C_{m,n}^2(n)$ is long spectral tails, which are omitted in the figures, but which make a significant contribution to the calculation of information entropy. Truncation of a topologically neutral beam ($m = 0$) with a circular aperture in **Figure 9(Ia)** leads to overlapping many side rings, resulting in a wave-like form of the spectral tail. In the perturbed vortex beams shown in **Figure 9(Ibc)**, a broadening of the vortex spectrum and a decrease in the tail amplitudes are observed. Such characteristic features of the vortex spectra insert significant uncertainty into information carried by the vortex beam, which is represented as the dependence of information entropy H_I on the aperture radius R_0 in **Figure 9(Id)**. It is noteworthy that even small variations in the aperture radius lead to changes in the entropy H_I that grow with increasing TC. Similar changes in the entropy $H_I(h)$ shown in **Figure 9(IId)** occur when a vortex beam is perturbed

by a annular aperture, which are the result of transformations in the vortex spectra in **Figure 9(a–c)**. The presented results show that any external interference in the beam immediately affects the uncertainty of the vortex beam state, the magnitude of which can be estimated by measuring informational entropy.

Another interesting feature of the axial aperture action is manifested under the combined vortex beam perturbation consisting of two vortex beams with the same values but different TC signs (m and $-m$). If the amplitudes of the beams are the same, then the complex amplitude of such a combined beam is described by Eq. (28) when replacing the phase factor $\exp(im\varphi) \to 2\cos m\varphi$. **Figure 10(b–d)** illustrates the intensity distribution of such perturbed beams at the measurement plane. Each of these beams receives the same perturbations, regardless of the sign of their TC. Even if the beam amplitudes are different, they receive the same amount of the vortex state uncertainty. However, this apparent indistinguishability of the modes can be easily detected experimentally due to opposite phase circulation of the fields, and the modes can be sorted out in different memory cells.

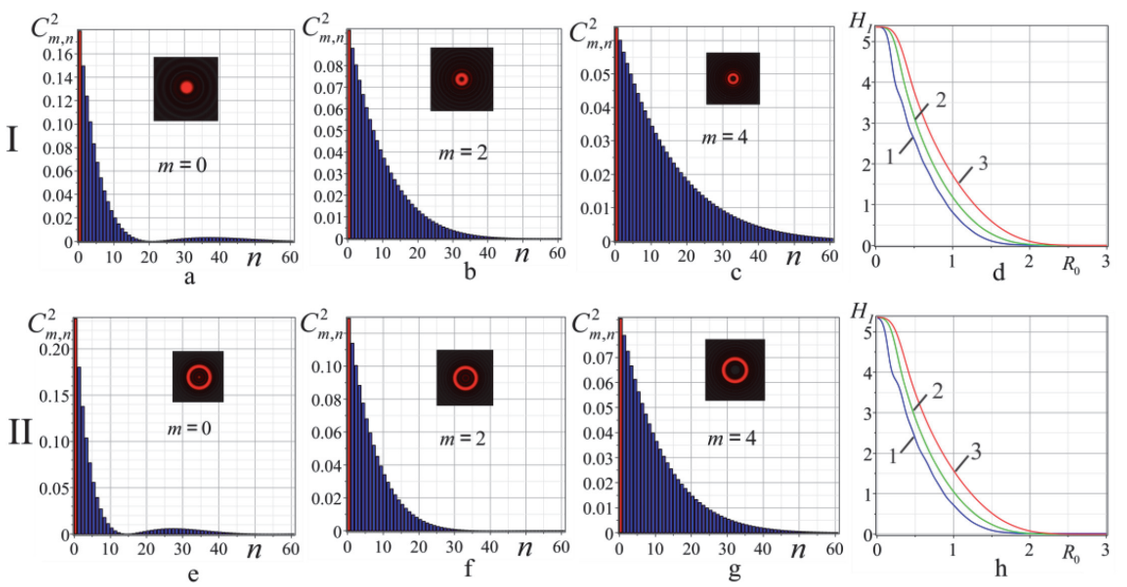

Figure 9.
The vortex spectra $C^2_{m,n}$ and the Shannon entropy $H_I(h)$ of the perturbed singular beams with different TC m: (I) the circular aperture; (II) the annular aperture; (Id) the Shannon entropy H_I via the aperture radius R_0; (IIh) the Shannon entropy H_I via the annular width, curves 1 and 3 correspond to the TC $m = 0, m = 2, m = 4$, respectively; callouts: corresponding intensity distributions.

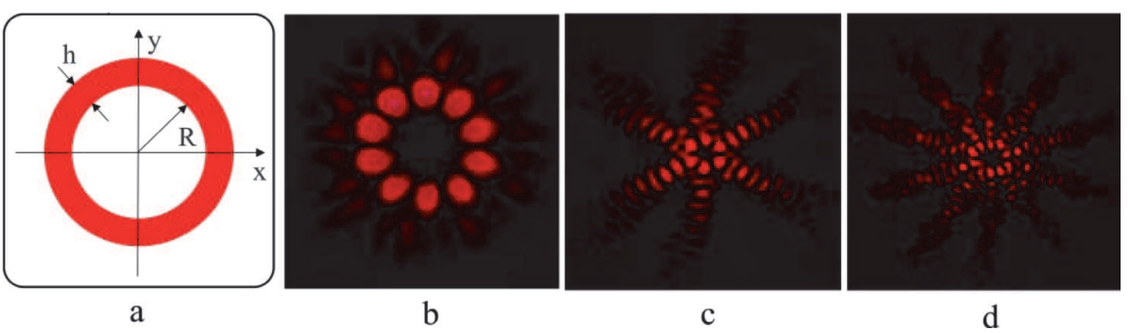

Figure 10.
(a) Sketch of the annular aperture. (b–d) Intensity distributions of the singular beams with TC $m = 5$ and $m = -5$ perturbed by the circular aperture with the radius (b) $R_0 = 0.5$, (c) $R_0 = 0.1$ and (d) the annular aperture with $R_0 = 0.5, h = 0.2$.

5. Conclusions

We examined the technique of digital sorting of vortex modes that makes it possible to measure in real time the vortex spectrum (squared amplitudes and initial phases) including radial indices, OAM, and informational entropy of perturbed singular beams. The considered approach is based on the measurement of intensity moments of higher orders and a digital solution of a linear equations system that eliminates the cuts and gluing of the beam wavefront without losing information on the modes initial phases. Moreover, the digital vortex spectrum also enables us to restore the initial combined beam and, correcting parameters of the spectral modes, to improve its characteristics.

The digital approach has been tested on vortex beams free of wave defects perturbed both by local defects of holographic gratings responsible for the beam generation and by the sectorial, circular and annular aperture. We revealed that a local perturbation of the holographic grating near the central forked defect causes bursts and dips in the OAM spectrum. The depth and height of the spectral dips and bursts are controlled by the parameters of the holographic grating and can vary over a wide range. The perturbation inserted by the sector aperture is regulated by the sector angle. Over a wide range of sector angles, the beam OAM remains almost unchanged. However, when the sector angle is relatively large, so that most of the light flux is cut off by the aperture, the optical uncertainty principle begins to act, and the OAM sharply decreases to almost zero that is accompanied by a rapid growth of the Shannon entropy. At the same time, the beam topological charge remains unchanged for any sectorial perturbations. The axial perturbation via a circular and annular aperture does not change either the OAM or topological charge. However, a wide range of Laguerre-Gauss modes with the same topological charges but different radial indices leads to a rapid increase in information entropy as the pupil of the circular aperture or the ring thickness of the annular aperture decreases. This allows not only to estimate the noise level in the optical information transmission line, but also to record external interference in the information flow. We also note that the digital sorting of optical vortices in a perturbed light flux opens up broad prospects for its employment for medical express-diagnostics of skin diseases, since, for example, this allows us to detect slight changes in the vortex spectrum of a laser beam scattered by inflamed or dehydrated skin areas.

Acknowledgements

The authors are grateful to E. Abramochkin (Samara Branch of the Lebedev Physical Institute, Russian Academy of Sciences, Samara, Russia) for a useful discussion of the mathematical approach. The reported study was funded by RFBR according to the research project № 19-29-01233.

IntechOpen

Author details

Alexander Volyar*, Mikhail Bretsko, Yana Akimova and Yuriy Egorov
Physics and Technology Institute, V.I. Vernadsky Crimean Federal University, Simferopol, Republic of Crimea, Russia

*Address all correspondence to: volyar@singular-optics.org

References

[1] Allen L, Beijersbergen MW, Spreeuw RJC, Woerdman JP. Orbital angular momentum of light and the transformation of Laguerre-Gaussian laser modes. Physical Review A. 1992; **45**(11):8185-8189. DOI: 10.1103/PhysRevA.45.8185

[2] Berry M. Nature's optics and our understanding of light. Contemporary Physics. 2015;**56**(1):2-16. DOI: 10.1080/00107514.2015.97162

[3] Mendenhall MJ, Nunez AS, Martin RK. Human skin detection in the visible and near infrared. Applied Optics. 2015;**51**(2):10559-10570. DOI: 10.1364/AO.54.010559

[4] Michel AP, Liakat S, Bors K, Gmachl CF. In vivo measurement of mid-infrared light scattering from human skin. Biomedical Optics Express. 2013;**4**(4):520-530. DOI: 10.1364/BOE.4.000520

[5] Chorvat D, Chorvatova A. Multi-wavelength fluorescence lifetime spectroscopy: A new approach to the study of endogenous fluorescence in living cells and tissues. Laser Physics Letters. 2009;**6**:175-193. DOI: 10.1002/lapl.200810132

[6] Gbur GJ. Singular Optics. New York: CRC Press; 2017. DOI: 10.1201/9781315374260

[7] Lavery MPJ, Berkhout GCG, Courtial J, Padgett MJ. Measurement of the light orbital angular momentum spectrum using an optical geometric transformation. Journal of Optics. 2013; **13**:064006. DOI: 10.1088/2040-8978/13/6/064006

[8] Shen Y, Yang X, Qi R, Wan Z, Fu X, Gon M. Recent advances on tunable vortex beam devices for biomedical applications. BJSTR. 2018;**9**(3):2/5-4/5. DOI: 10.26717/BJSTR.2018.09.001801

[9] Otaka H, Shimakura H, Motoyoshi I. Perception of human skin conditions and image statistics. Journal of the Optical Society of America A. 2019; **36**(9):1609-1616. DOI: 10.1364/JOSAA.36.001609

[10] Ney M, Abdulhalim I. Does human skin truly behave as an array of helical antennae in the millimeter and terahertz wave ranges? Optics Letters. 2010; **35**(19):3180-3182. DOI: 10.1364/OL.35.003180

[11] Gbur G, Korotkova O. Angular spectrum representation for the propagation of arbitrary coherent and partially coherent beams through atmospheric turbulence. Journal of the Optical Society of America. A. 2007;**24**: 745-752. DOI: 10.1364/JOSAA.24.000745

[12] Soifer VA, Korotkova O, Khonina SN, Shchepakina EA. Vortex beams in turbulent media. Review Computer Optics. 2016;**40**(5):605-621. DOI: 10.18287/2412-6179-2016-40-5-605-624

[13] Majumdar A, Kirkpatrick SJ. Statistical studies on optical vortices in dynamic speckle fields. Journal of Biomedical Photonics & Engineering. 2018;**4**(2):020301-1-020301-9. DOI: 10.18287/JBPE18.04.020301

[14] Reddy SG, Prabhakar S, Kumar A, Banerji J, Singh RP. Higher order optical vortices and formation of speckles. Optics Letters. 2014;**39**(15):4364-4367. DOI: 10.1364/OL.39.004364

[15] Kirkpatrick SJ, Khaksari K, Thomas D, Duncan DD. Optical vortex behavior in dynamic speckle fields. Journal of Biomedical Optics. 2012; **17**(5):050504-1-050504-3. DOI: 10.1117/1.JBO.17.5.050504

[16] Machado FJ, Monsoriu JA, Furlan WD. Fractal light vortices. In:

Perez-de-Tejada H, editor. Vortex Dynamics and Optical Vortices. Rijeka: IntechOpen; 2017. DOI: 10.5772/66343

[17] Segev M, Soljačić M, Dudley JM. Fractal optics and beyond. Nature Photonics. 2012;**6**(4):209-210. DOI: 10.1038/nphoton.2012.71

[18] Sheppard CJR. Fractal model of light scattering in biological tissue and cells. Optics Letters. 2007;**32**(2):142-144. DOI: 10.1364/OL.32.000142

[19] Xu M, Alfano RR. Fractal mechanisms of light scattering in biological tissue and cells. Optics Letters. 2005;**30**(22):3051-3053. DOI: 10.1364/OL.30.003051

[20] Si K, Gong W, Sheppard CJR. Model for light scattering in biological tissue and cells based on random rough nonspherical particles. Applied Optics. 2009;**48**(6):1153-1157. DOI: 10.1364/AO.48.001153

[21] Khonina SN, Kotlyar VV, Soifer VA, Paakkonen P, Turunen J. Measuring the light field orbital angular momentum using DOE. Optical Memory and Neural Networks. 2001;**10**(4):241-255

[22] Khonina SN, Kotlyar VV, Soifer VA, Jefimovs K, Turunen J. Generation and selection of laser beams represented by a superposition of two angular harmonics. Journal of Modern Optics. 2004;**51**: 761-773. DOI: 10.1080/09500340408235551

[23] Khonina SN, Kazanskiy NL, Soifer VA. In: Yasin M, Harun SW, Arof H, editors. Optical Vortices in a Fiber: Mode Division Multiplexing and Multimode Self-Imaging, Recent Progress in Optical Fiber Research. Rijeka: IntechOpen; 2012. DOI: 10.5772/28067

[24] Berkhout GCG, Lavery MPJ, Courtial J, Beijersbergen MW, Padgett MJ. Efficient sorting of orbital angular momentum states of light. Physical Review Letters. 2010;**105**: 153601. DOI: PhysRevLett.105.153601

[25] Volyar A, Bretsko M, Akimova Y, Egorov Y. Measurement of the vortex spectrum in a vortex-beam array without cuts and gluing of the wavefront. Optics Letters. 2018;**43**(22): 5635-5638. DOI: 10.1364/OL.43.005635

[26] Alperin SN, Niederiter RD, Gopinath JT, Siements KE. Quantitative measurement of the orbital angular momentum of light with a single, stationary lens. Optics Letters. 2016;**41**: 5019-5022. DOI: 10.1364/OL.41.005019

[27] Alperin N, Siemens ME. Angular momentum of topologically structured darkness. Physical Review Letters. 2017; **119**:203902. DOI: PhysRevLett.119.203902

[28] Kotlyar VV, Kovalev AA, Porfirev AP. Methods for determining the orbital angular momentum of a laser beam. Computer Optics. 2019;**43**(1): 42-53. DOI: 10.18287/2412-6179-2019-43-1-42-53

[29] Soifer VA, Golub MA. Laser Beam Mode Selection by Computer-Generated Holograms. Boca Raton: CRC Press; 1994. p. 224. ISBN: 978-0-8493-2476-5

[30] Gibson G, Courtial J, Padgett MJ, Vasnetsov M, Pas'ko V, Barnett SM, et al. Free-space information transfer using light beams carrying orbital angular momentum. Optics Express. 2004;**12**:5448-5456

[31] Berry MV. Paraxial beams of spinning light. In: Proceedings of the SPIE International Conference Singular Optics. Vol. 3487. 1998. pp. 6-11. DOI: 10.1117/12.317704

[32] D'errico A, D'amelio R, Piccirillo B, Cardano F, Marrucc L. Measuring the complex orbital angular momentum spectrum and spatial mode

decomposition of structured light beams. Optica. 2017;**4**:1350-1357

[33] Andersen JM, Alperin SN, Voitev AA, Holtzmann WG, Gopinath JT, Simens ME. Characterizing vortex beams from a spatial light modulator with collinear phase-shifting holography. Applied Optics. 2019;**58**: 404-409. DOI: 10.1364/AO.58.000404

[34] Kotlyar V, Kovalev A, Porfirev A. Calculation of fractional orbital angular momentum of superpositions of optical vortices by intensity moments. Optics Express. 2019;**27**(8):11236-11251. DOI: 10.1364/OE.27.011236

[35] Flusser J, Suk T, Zitová B. Moments and Moment Invariants in Pattern Recognition. John Wiley & Sons, Ltd: Chichester; 2009. p. 312. DOI: 10.1002/9780470684757

[36] Alexeyev CN, Egorov YA, Volyar AV. Mutual transformations of fractional-order and integer-order optical vortices. Physical Review A. 2017;**96**:063807. DOI: 10.1103/PhysRevA.96.063807

[37] Fu S, Gao C. Influences of atmospheric turbulence effects on the orbital angular momentum spectra of vortex beams. Photonics Research. 2016; **4**:B1-B4. DOI: 10.1364/PRJ.4.0000B1

[38] Kaiser T, Flamm D, Schroter S, Duparre M. Complete modal decomposition for optical fibers using CGH-based correlation filters. Optics Express. 2009;**17**:9347-9356. DOI: 10.1364/OE.17.009347

[39] Volyar A, Bretsko M, Akimova Y, Egorov Y. Measurement of the vortex and orbital angular momentum spectra with a single cylindrical lens. Applied Optics. 2019;**58**(21):5748-5755. DOI: 10.1364/AO.58.005748

[40] Abramochkin E, Razueva E, Volostnikov V. General astigmatic transform of Hermite–Laguerre–Gaussian beams. Journal of the Optical Society of America A. 2010;**27**: 2506-2513. DOI: 10.1364/JOSAA.27.002506

[41] Abramochkin E, Volostnikov V. Beam transformations and non-transformed beams. Optics Communications. 1991;**83**(12):123-135. DOI: 10.1016/0030-4018(91)90534-K

[42] Berry MV. Optical vortices evolving from helicoidal integer and fractional phase steps. Journal of Optics A. 2004;**6**: 259-268. DOI: 10.1088/1464-4258/6/2/018

[43] Fadeyeva TA, Rubass AF, Aleksandrov RV, Volyar AV. Does the optical angular momentum change smoothly in fractional-charged vortex beams? Journal of the Optical Society of America B: Optical Physics. 2014;**31**(4): 798-805. DOI: 10.1364/JOSAB.31.000798

[44] Götte B, O'Holleran K, Preece D, Flossmann F, Franke-Arnold S, Barnett SM, et al. Light beams with fractional orbital angular momentum and their vortex structure. Optics Express. 2008;**16**:993-1006. DOI: 10.1364/OE.16.000993

[45] Gutiérrez-Vega JC, López-Mariscal C. Nondiffracting vortex beams with continuous orbital angular momentum order dependence. Journal of Optics A. 2008;**10**:015009. DOI: 10.1088/1464-4258/10/01/015009

[46] Nemes G, Siegman A. Measurement of all ten second-order moments of an astigmatic beam by the use of rotating simple astigmatic (anamorphic) optics. Journal of the Optical Society of America. A. 1994;**11**:2257. DOI: 10.1364/JOSAA.11.002257

[47] Volyar A, Bretsko M, Akimova Y, Egorov Y. Vortex avalanche in the perturbed singular beams. Journal of the

Optical Society of America A. 2019; **36**(6):1064-1071. DOI: 10.1364/JOSAA.36.001064

[48] Volyar A, Egorov Y. Super pulses of orbital angular momentum in fractional-order spiroid vortex beams. Optics Letters. 2018;**43**(1):74-77. DOI: 10.1364/OL.43.000074

[49] Volyar A, Bretsko M, Akimova Y, Egorov Y. Orbital angular momentum and informational entropy in perturbed vortex beams. Optics Letters. 2019; **44**(23):5687-5690. DOI: 10.1364/OL.44.005687

[50] Yao E, Franke-Arnold S, Courtial J, Barnett S, Padgett M. Fourier relationship between angular position and optical orbital angular momentum. Optics Express. 2006;**14**:9071-9076. DOI: 10.1364/OE.14.009071

[51] Yu FTS. Entropy and Information Optics. Boca Raton: CRC Press; 2000. 360 p. DOI: 10.1201/9781315214498

[52] Volyar A, Bretsko M, Akimova Y, Egorov Y, Milyukov V. Sectorial perturbation of vortex beams: Shannon entropy, orbital angular momentum and topological charge. Computer Optics. 2019;**43**(5):722-733. DOI: 10.18287/2412-6179-2019-43-5-723-734

[53] Born M, Wolf E. Principles of Optics. 7th ed. London: Cambridge University Press; 1999. 952 p. DOI: 10.1017/CBO9781139644181

[54] Karimi E, Giovannini D, Bolduc E, Bent N, Miatto FM, Padgett MJ, et al. Exploring the quantum nature of the radial degree of freedom of a photon via Hong-Ou-Mandel interference. Physical Review A. 2014;**89**:013829-1-013829-5. DOI: 10.1103/PhysRevA.89.013829

[55] Bouchard F, Herrera-Valencia N, Brandt F, Fickler R, Huber M, Malik M. Measuring azimuthal and radial modes of photons. Optics Express. 2018; **26**(24):31925-31941. DOI: 10.1364/OE.26.031925

[56] Prudnikov AP, Brychkov YA, Marichev OI. Integrals and Series. Special Functions. New York: Gordon and Breach; 1986. p. 798. ISBN: 2881240909 9782881240904